Morphological and Crystalline Evolution of Nanostructured MnO_2 and Its Application in Lithium–Air Batteries

Tu T. Truong,[†] Yuzi Liu,[†] Yang Ren,[‡] Lynn Trahey,[§] and Yugang Sun[†,*]

[†]Center for Nanoscale Materials, [‡]X-ray Science Division, Advanced Photon Source, and [§]Chemical Sciences and Engineering Division, Argonne National Laboratory, 9700 South Cass Avenue, Argonne, Illinois, 60439, United States

ABSTRACT Single-crystal α-MnO_2 nanotubes have been successfully synthesized by microwave-assisted hydrothermal of potassium permanganate in the presence of hydrochloric acid. The growth mechanism including the morphological and crystalline evolution has been carefully studied with time-dependent X-ray diffraction, electron microscopy, and controlled synthesis. The as-synthesized MnO_2 nanostructures are incorporated in air cathodes of lithium–air batteries as electrocatalysts for the oxygen reduction and evolution reactions. The characterization reveals that the electrodes made of single-crystalline α-MnO_2 nanotubes exhibit much better stability than those made of α-MnO_2 nanowires and δ-MnO_2 nanosheet-based microflowers in both charge and discharge processes.

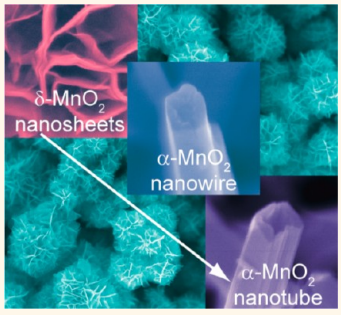

KEYWORDS: microwave synthesis · nanostructured manganese oxide · morphological control · electrochemical catalyst · lithium–air batteries

Nanostructured manganese dioxides (MnO_2) are among the promising materials for high-performance electrochemical energy storage devices including high-capacity lithium-ion batteries,[1−3] lithium–air batteries,[4−7] and supercapacitors[8,9] that represent the high demand for use in electric vehicles and other consumer electronics.[10−12] The use of MnO_2 nanomaterials as active electrode components in energy storage devices has many advantages in terms of their high specific energy capacity, low fabrication cost, abundance of the materials in the earth, and environmentally friendly nature.[8,13,14] Intensive studies in the past have proven that the performance of electrochemical devices is strongly affected by the crystalline phase and morphology of MnO_2 nanostructures that depend on the synthetic strategy and reaction conditions.[13] For instance, various methods including coprecipitation,[15] sol–gel technique,[16] hydrothermal reaction,[17,18] *etc.* have been used for the synthesis of nanostructured MnO_2 with various morphologies such as plates,[19] urchin-like structures,[3,20] spheres,[21,22] flowers,[23] cubes,[24] wires,[25,26] rods,[27] belts,[28] tubes,[29−31] *etc.* The as-synthesized MnO_2 nanostructures can be crystallized in different phases (*e.g.*, α, β, δ, γ, and λ) depending on how the repeated MnO_6 octahedron units in MnO_2 share their faces and edges. The morphological and structural complexity of MnO_2 nanostructures makes the synthesis of MnO_2 nanomaterials with highly pure crystallographic phases and uniform morphology to be challenging. On the other hand, the availability of pure phase MnO_2 nanomaterials is essential for investigating the correlation between the physical parameters of the MnO_2 nanoparticles and device performance. Herein, we report the use of a microwave-assisted hydrothermal method to synthesize MnO_2 nanostructures with well-controlled morphology and crystallinity in high uniformity and purity. The use of microwaves to drive solution-phase reactions offers many advantages in comparison with conventional heating processes, for example, prompt start-up, uniform temperature distribution in reaction solutions, efficient energy conversion and delivery, easy control over reaction conditions, and possible scaling up.[32−34] By appropriately controlling the reaction conditions, we successfully synthesized uniform δ-MnO_2 microflowers consisting of assemblies of nanosheets, α-MnO_2 nanowires, and α-MnO_2 nanotubes with open ends. The detailed morphological and crystalline evolutions have been studied at the atomic resolution with time-dependent X-ray diffraction, electron microscopy, and

* Address correspondence to ygsun@anl.gov.

Received for review June 15, 2012 and accepted August 6, 2012.

Published online August 06, 2012
10.1021/nn302654p

controlled synthesis. The as-synthesized MnO_2 nanostructures have been incorporated into air cathodes in lithium–air batteries to serve as catalysts for facilitating the electrochemical processes involving oxygen reduction and evolution reactions. The results indicate that the morphology and crystallinity of the MnO_2 nanostructures indeed influence the performance of the lithium–air batteries and the α-MnO_2 nanotubes represent the best in terms of energy capacity and stability.

RESULTS AND DISCUSSION

The synthesis of MnO_2 nanostructures has been carried out through hydrothermal reactions between an aqueous solution of potassium permanganate ($KMnO_4$) and hydrochloric acid (HCl) in an aqueous solution at elevated temperatures that is achieved by heating the reaction solution with a microwave reactor. In a typical synthesis, an appropriate amount of concentrated HCl solution is first added to an aqueous solution of $KMnO_4$ in a microwave reaction vessel (*i.e.*, a glass tube specially manufactured for CEM Discover microwave reactor) at room temperature. The mixing process does not induce an apparent reaction. Once the reaction vessel is sealed, quickly heating the solution to 150 °C within 1 min with the microwave reactor triggers a redox reaction

$$2MnO_4^- + 8H^+ + 6Cl^- \rightarrow 2MnO_2 + 3Cl_2 + 4H_2O \quad (1)$$

because the reaction $MnO_4^- + 4H^+ + 3e^- \rightarrow MnO_2(s) + 2H_2O$ exhibits a higher standard electrode potential (1.70 V *versus* SHE, standard hydrogen electrode) than that of the reaction $Cl_2(g) + 2e^- \rightarrow 2Cl^-$ (1.36 V *versus* SHE). The release of Cl_2 gas can be confirmed by the following facts: an irritating odor can be smelt when a synthesis is completed and the reactor is opened; the copper pressure gauge head that holds the septum caps to seal the reactors during the hydrothermal reaction is found to be severely eroded after a number of syntheses are performed. The corrosion of the pressure gauge head is ascribed to its reaction with the Cl_2 gas released from reaction 1 that can penetrate through the septum caps to attack the pressure gauge head in humid atmosphere due to the high pressure built in the reaction vessels. As highlighted in reaction 1, both Cl^- ions and H^+ ions play important roles to drive the reaction where Cl^- ions are a reducing species to reduce MnO_4^- ions to form MnO_2 solids and H^+ ions provide an acidic environment to promote the redox reaction. When the reaction solution is neutral, no apparent reaction occurs. For example, there are no MnO_2 solids formed in a reaction solution containing $KMnO_4$ and NaCl. In contrast, the formation of MnO_2 solids can also be boosted by adding H_2SO_4 to the solution of $KMnO_4$ and NaCl, confirming the importance of high acidity on accelerating the reaction kinetics. In addition to the redox reaction shown in eq 1, decomposition of MnO_4^- ions possibly occurs simultaneously to form MnO_2 solids in an acidic solution:

$$4MnO_4^- + 4H^+ \rightarrow 4MnO_2 + 3O_2 + 2H_2O \quad (2)$$

because black MnO_2 powders can also be formed from direct heating of an aqueous solution of $KMnO_4$ and H_2SO_4. However the reaction rate for producing MnO_2 is much lower than that from the reaction solution of $KMnO_4$ and HCl. Moreover, the MnO_2 powders that resulted from the solution of $KMnO_4$ and H_2SO_4 exhibit morphologies (bundles of thinner wires) different from those from the reaction between $KMnO_4$ and HCl. Comparison of the different reactions indicates that both reaction 1 and reaction 2 contribute to the formation of MnO_2 powders although the significance of individual reactions may be different. Apparently the contribution of reaction 1 is more significant in the solution of $KMnO_4$ and HCl.

The reaction between $KMnO_4$ and HCl is fast, leading to the formation of precipitated black MnO_2 powders within several minutes. Figure 1A shows a scanning electron microscopy (SEM) image of the powders formed at the very beginning of the reaction, that is, 2 min that is normalized against the time when the temperature reaches 150 °C. The image clearly shows the formation of desert rose-like microflowers constructed with intersected nanosheets. As the reaction proceeds, the purple color of the reaction solution gradually diminishes, indicating that the MnO_4^- ions are reduced to form solid MnO_2. Absorption spectroscopic investigation reveals that the reduction of MnO_4^- ions completes within 5 min after the reaction temperature reaches 150 °C (Figure S1, Supporting Information). The product formed at 5 min is shown in Figure 1B with a slight increase in size of the microflowers. Continuously heating the microflowers under the hydrothermal condition gradually changes the morphologies of the resulting nanostructures. As shown in Figure 1C, a number of nanowires grow from the flowers at 15 min, indicating a possible phase transition of the MnO_2 microflowers occurs under the reaction condition. Once the morphological transformation is initiated, the microflowers can be converted to nanowires quickly; for example, the product formed at 30 min exhibits pure nanowires with diameters of ~100 nm (Figure 1D). Further annealing of the nanowires transforms them into hollow nanotubes with open ends (Figure 1E,F, and Supporting Information Figure S2). These sequential morphological changes indicate that the MnO_2 microflowers are in the form of a metastable phase under the reaction condition. The X-ray diffraction (XRD) pattern of the flowers formed at 2 min exhibits the characteristic diffraction peaks corresponding to the pure δ-phase MnO_2 (Figure 2A). The (001) and (002) peaks correspond to the layered structure of δ-MnO_2. XRD patterns of the nanowires and nanotubes formed at times longer than 30 min indicate these one-dimensional

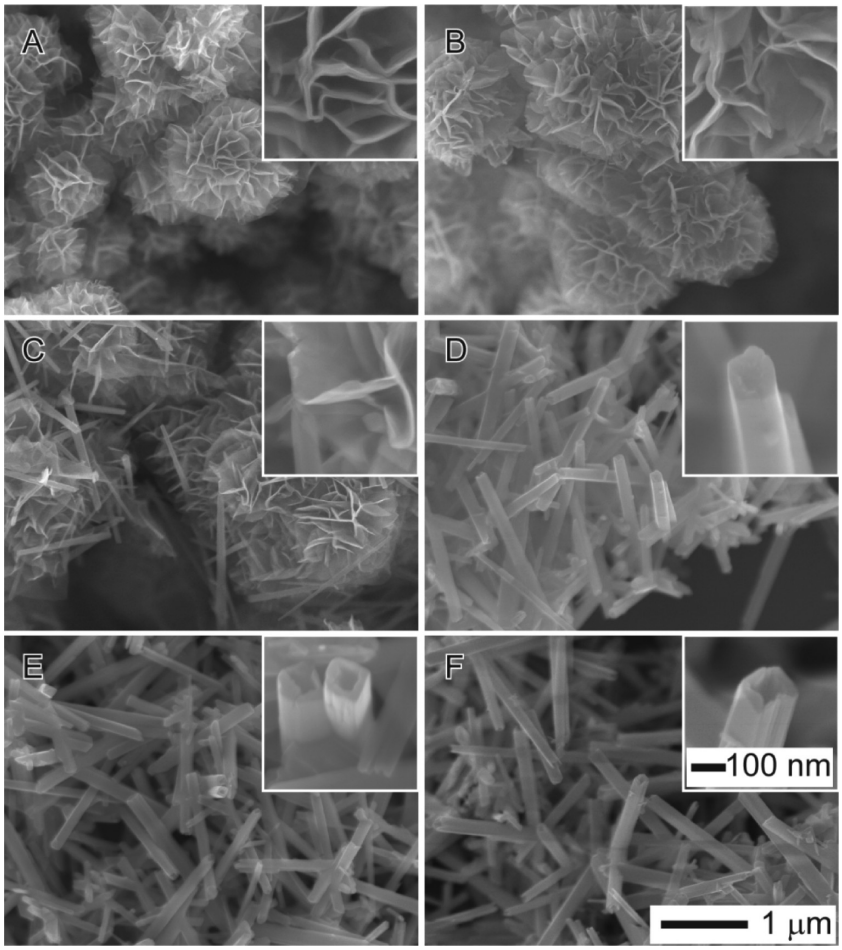

Figure 1. SEM images of MnO_2 products obtained at different reaction times: (A) 2, (B) 5, (C) 15, (D) 30, (E) 120, and (F) 360 min. The temperature of the reaction solutions and the atmosphere pressure above the reaction solutions were 150 °C and 70 psi, respectively. The concentrations of $KMnO_4$ and HCl in the reaction solution were 0.05 and 0.2 M, respectively, before the reaction was initiated. The insets are the high-magnification SEM images of the corresponding structures. The scale bars in F also apply to A−E.

nanostructures are made of α-phase MnO_2 (Figure 2A). The phase transition from δ-MnO_2 microflowers to α-MnO_2 nanowires/nanotubes is consistent with the XRD pattern of the product formed in 15 min that exhibits diffraction peaks of both δ- and α-MnO_2 (cyan curve, Figure 2A). The phase transition of MnO_2 nanostructures from the δ-phase to α-phase indicates that the layered crystalline structure tends to convert into the 2 × 2 channeled crystalline structure under the reaction conditions (Figure 2B). These observations indicate that microflowers with pure δ-MnO_2, nanowires with pure α-MnO_2, and nanotubes with pure α-MnO_2 can be readily synthesized through the microwave-assisted hydrothermal approach by simply controlling the reaction time.

Characterization of MnO_2 Nanostructures with TEM and Electron Diffraction. Transmission electron microscopy (TEM) and electron diffraction have been used to study the detailed crystalline structures of MnO_2 nanostructures at the atomic level. Figure 3 presents the TEM images and selected area electron diffraction (SAED) pattern of a MnO_2 microflower formed at the very early stage of the reaction (*i.e.*, 2 min). Similar to the SEM image shown in Figure 1A, the TEM image also shows that the microflower is an assembly of nanosheets with very thin thickness that is consistent with the low image contrast of individual nanosheets at the edge of the flower. The thin nanosheets tend to curl and fold, resulting in the opportunity for us to directly measure their thickness from the vertical edges shown in Figure 3B. The typical thickness of the nanosheets is 3−4 nm. The high-resolution TEM (HRTEM) image of the edge (Figure 3B) shows lattice fringes (highlighted by the lines) with spacing of ~7.1 Å that corresponds to the (001) lattice of δ-MnO_2. The HRTEM images recorded by aligning the electron beam perpendicular to the basal surfaces of individual nanosheets show that each nanosheet is polycrystalline and consists of many tiny grains with sizes of 2−10 nm (Figure 3C). The observed lattice fringes along this direction exhibit the same spacing of ~2.4 Å which corresponds to the (−111) lattice of δ-MnO_2. The appearance of (−111) lattice fringes is consistent with the SAED pattern (Figure 3D) over the area highlighted by the circle in Figure 3A. Another diffraction ring originated from the

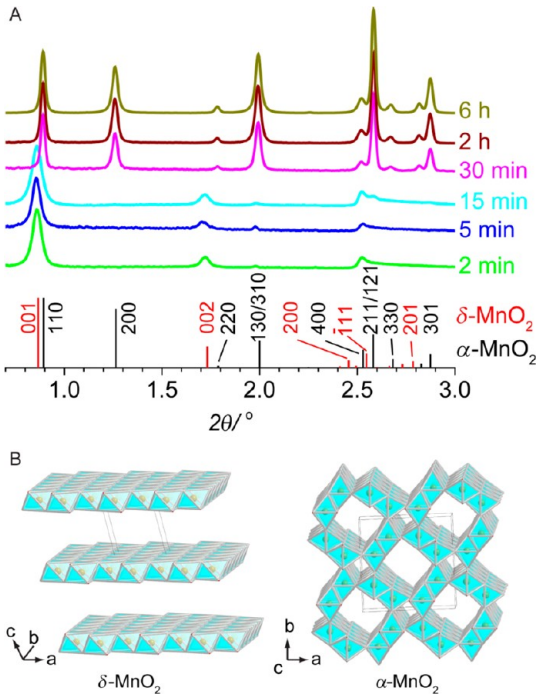

Figure 2. (A) XRD patterns of the MnO_2 products shown in Figure 1. The sticks highlight the peak positions and relative peak intensities of the standard powder XRD patterns of α-MnO_2 (black) and δ-MnO_2 (red) for reference. Wavelength of the X-ray beam was 0.10798 Å. (B) Schematic illustrations of crystal structures of δ-MnO_2 and α-MnO_2 (tetragonal with *a* = 9.8 Å, and *c* = 2.9 Å).

(020) reflection of δ-MnO_2 is also observed in the SAED pattern, although the corresponding lattice fringes are not observed in the HRTEM image (Figure 3C) due to the limited spatial resolution of the TEM. The absence of diffraction rings of (001) and (002) of δ-MnO_2 in the SAED pattern is attributed to the fact that the possibility of the nanosheet surfaces parallel to the electron beam as shown in Figure 3B is very low and the corresponding contribution to the SAED pattern cannot be detected.

As discussed previously, the δ-MnO_2 crystalline nanodomains are not stable under the reaction conditions, and they are transformed into α-MnO_2 nanowires. Figure 4 presents the characterization results of the sample formed at 15 min. The typical TEM image clearly shows the existence of both nanosheets and nanowires in the sample, indicating that the δ-MnO_2 microflowers are partially converted to α-MnO_2 nanowires. The nanowires are entangled with the nanosheets of the original microflowers. Each nanowire has its one end embedded in the nanosheets, indicating that the growth of the α-MnO_2 nanowire is initiated by the formation of α-MnO_2 nucleus in a δ-MnO_2 nanosheet followed by an anisotropic growth. During the phase transition process, the edges of the δ-MnO_2 nanosheets become rough in comparison with those of the original microflowers (Figure 4B *versus* Figure 3C). The change of the edge profile of the nanosheets indicates that the δ-MnO_2 nanodomains are gradually detached from the nanosheets under the reaction conditions. From these observations, we can conclude that once α-MnO_2 nuclei are formed, the tiny δ-MnO_2 nanodomains in the nanosheets will diffuse to the thermodynamically stable α-MnO_2 nuclei to help them grow into nanowires. The SAED pattern of the roughed nanosheets still exhibits diffraction rings consistent with the δ-MnO_2, indicating that the δ-MnO_2 to α-MnO_2 phase transition occurs on the α-MnO_2 nuclei and the derived nanowires. HRTEM images recorded from the central portion of a nanowire exhibit continuous lattice fringes with spacing of ~4.8 Å which corresponds to the (200) lattice of α-MnO_2 (Figure 4C). The corresponding SAED pattern agrees the pattern of single crystalline α-MnO_2 with [011] zone axis (Figure 4D). The stretched shapes of the reflection spots indicate that there are numerous stacking faults along the nanowire. The contrast variation in Figure 4C means there are small α-MnO_2 crystalline domains embedded in the nanowire. In contrast, the HRTEM image of the end of the nanowire clearly shows a core/shell structure (Figure 4E). The shell has a thin wall with continuous lattice fringes with spacings of ~4.8 Å that corresponds to the (200) lattice of α-MnO_2. The core is composed of many individual crystalline domains with lattice fringes that are difficult to assign to either pure α-MnO_2 or δ-MnO_2, indicating that the phase transition from δ-MnO_2 to α-MnO_2 nanodomains occurs in the nanowires rather in the δ-MnO_2 nanosheets. These intermediate domains in the nanowire may account for the extremely stretched reflection spots shown in the SAED pattern of Figure 4F. Apparently, the forefront profile of the nanowire's end is very rough while the side surfaces of the nanowire are smooth. The surface roughness and polycrystallinity prompts the reactivity of the end surface toward the attachment of additional MnO_2 domains that are diffused from the δ-MnO_2, leading to a continuous growth of the nanowire. The side surfaces of the nanowire are less reactive due to their smoothness and continuous lattices. In addition, the lattices of the α-MnO_2 nanowires exhibit an anisotropic crystallographic space group symmetry (*i.e.*, *I*4/*m*) with their longitudinal axes along the [0$\bar{1}$1] crystalline direction with a corresponding interplanar distance of 6.92 Å. This value is very close to the interplanar distance along the (001) direction in δ-MnO_2 (*i.e.*, 7.14 Å), leading to a preference to directly attach δ-MnO_2 nanodomains to the {110} facets of the α-MnO_2 nanowires *via* a quasi-epitaxial oriented attachment. In contrast, the interplanar distance along the side surfaces of the α-MnO_2 nanowires is 4.89 Å (corresponding to the (200) reflection in the XRD pattern shown in Figure 2A) that is significantly different from the interplanar distance along any crystalline direction in δ-MnO_2. Such mismatch prevents the nanowires from growing fatter. According to these discussions, it is understandable why the nanowires anistropically grow in one-dimensional fashion rather than three-dimensional fashion.

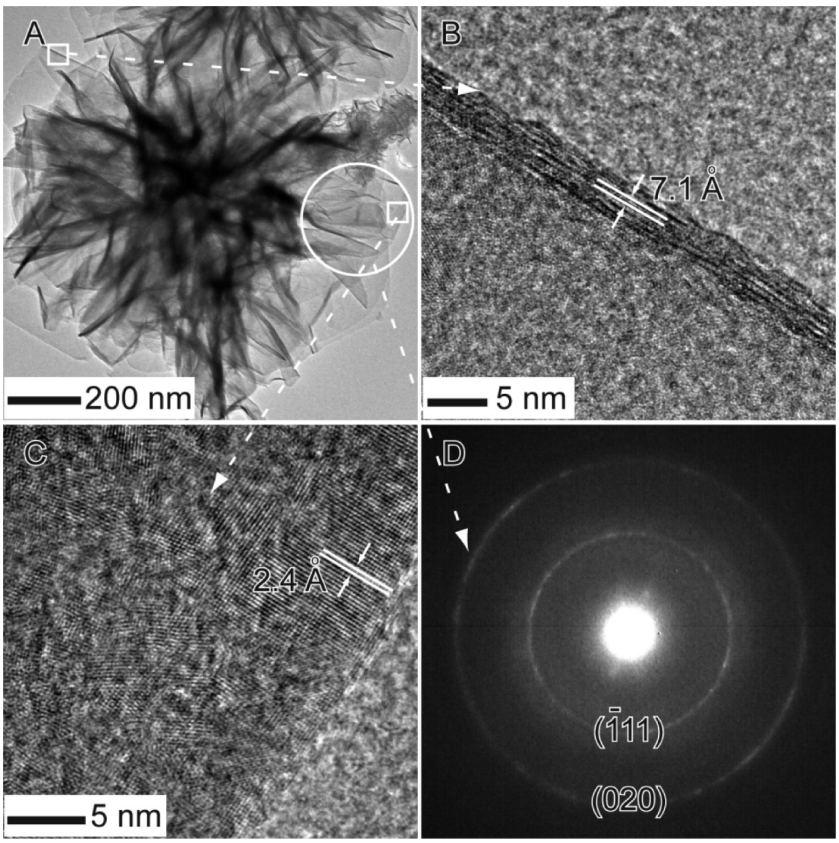

Figure 3. Characterization of an individual δ-MnO_2 microflower made of nanosheets that was obtained at 2 min. (A) Regular and (B, C) high-resolution TEM images of the microflower and its nanosheets. (D) SAED pattern recorded by focusing the electron beam in the area highlighted by the circle in image A.

As shown in Figure 1, the nanosheet-based microflowers are completely converted to nanowires at 30 min. As the reaction time is long enough (*i.e.*, >2 h), the solid nanowires are transformed into hollow nanotubes. Figure 5 presents the characterization results of the MnO_2 nanotubes formed at 6 h. Each nanotube has a rounded end that is closed (Figure 5B) and a steep end that is open (Figure 5C). As a result, each MnO_2 nanotube exhibits the geometry of a test tube. The lattice fringes parallel to the longitudinal axes of the nanotubes have a spacing of ~4.8 Å corresponding to the (200) lattice of α-MnO_2. The growth direction of the nanotubes is determined as $[0\bar{1}1]$ of α-MnO_2. The SAED patterns recorded at different spots of an individual nanotube are essentially the same as shown in Figure 5D which is consistent with the typical electron diffraction pattern of a single crystalline α-MnO_2. In comparison with the SAED patterns shown in Figure 4 for the solid nanowires, the reflection spots in Figure 5D are more symmetric. Also, in comparison to Figure 4 images C and E, the contrast in Figure 5 images B and C is more uniform. This means the small crystalline domains in the solid core/shell nanowires have fused with the single crystalline shells, leading to the formation of single-crystalline nanotubes.

Influence of Reaction Conditions. Reaction kinetics is significantly influenced by the reaction conditions including temperature, precursor concentration, *etc.* and thus the morphology and crystallinity of the resulting MnO_2 nanostructures vary under different reaction conditions. For example, Figure S3 (Supporting Information) presents SEM images and XRD patterns of the MnO_2 particles formed after 6 h at different temperatures, clearly showing the dependence of their morphology and crystalline phase on temperature. When the temperature is too low, such as 100 °C, the nanosheet-based δ-MnO_2 microflowers cannot be converted to α-MnO_2 nanowires/nanotubes (Figure S3A, Supporting Information), indicating that the δ- to α-MnO_2 phase transition requires a temperature higher than 100 °C. As the temperature increases to 130 °C, the reaction can completely convert the δ-MnO_2 microflowers into pure α-MnO_2 products (blue curve, Figure S3C, Supporting Information). Figure S3B (Supporting Information) shows the formation of nanowires with very small openings at their ends, indicating that 130 °C is still too low to drive the hollowing process to form nanotubes as shown in Figure 1F that are synthesized at 150 °C. As a result, maintaining a high temperature (*e.g.*, 150 °C) is critical to promote the δ- to α-MnO_2 phase transition and ripening process for hollowing nanowires into single crystalline nanotubes.

Varying reaction temperature can change the atmosphere pressure above the reaction solutions in the sealed reaction vessels because both water and HCl

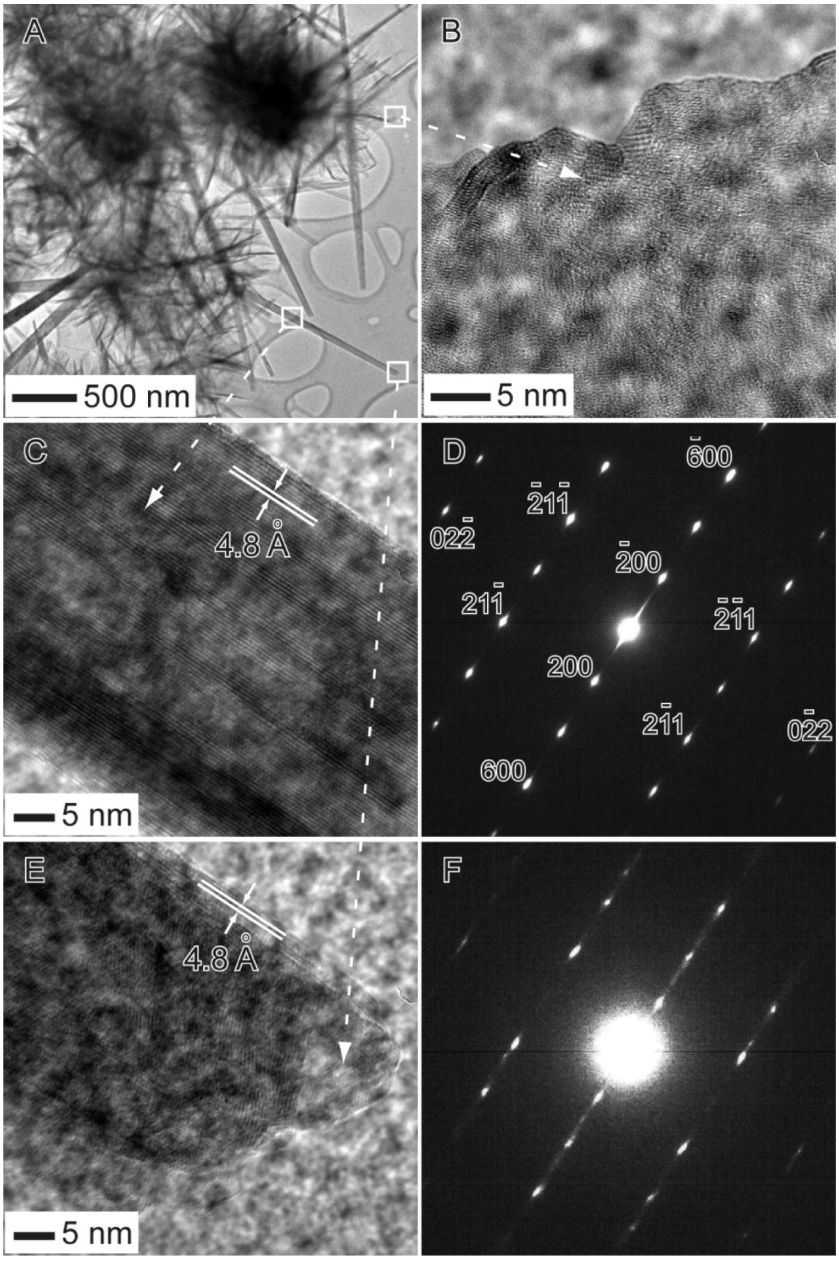

Figure 4. Characterization of the MnO_2 product formed at 15 min. (A) Regular TEM image of the sample. (B, C, E) HRTEM images taken from different areas highlighted by the squares in image A. Images D and F are the electron diffraction patterns corresponding to images C and E, respectively.

have different vapor pressures at different temperatures and the pressure contributions of Cl_2 and possible O_2 are also dependent on temperature. To check the influence of pressure, the volume ratio between the free space and solution in a reaction vessel is tuned while the concentrations of both $KMnO_4$ and HCl and the temperature remain the same as those in Figure 1. As shown in Figure S4 (Supporting Information), the final products synthesized after 6 h under different vapor pressures exhibit the same tube morphology and similar diameters. The consistency of MnO_2 nanotubes formed at different pressures indicates the pressure above the reaction solutions barely influences the chemical reactions and crystallization processes in the solutions. The independence of pressure might be because water is a condensed liquid and the pressure on the scale less than 6 atm cannot induce apparent influence on the behavior of the chemical species (*e.g.*, MnO_4^-, Cl^-, H^+, HCl, K^+, MnO_2 nanocrystals, *etc.*) in water. This result confirms that the variation of MnO_2 products shown in Figure S3 (Supporting Information) is mainly ascribed to the change of reaction temperature.

Hydrochloric acid plays an important role in the reduction of MnO_4^- ions into MnO_2 and modification of solution acidity. When the ratio of the concentration of HCl to that of MnO_4^- (*i.e.*, [HCl]/[MnO_4^-]) is much

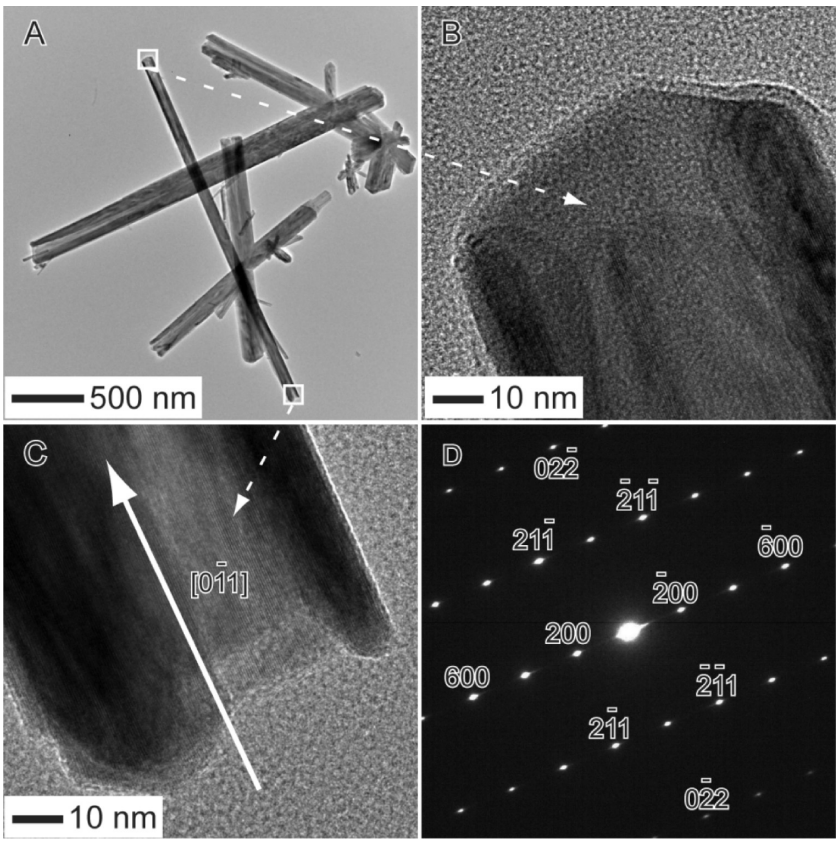

Figure 5. Characterization of the α-MnO_2 nanotubes formed at 6 h. (A) Regular and (B, C) high-resolution TEM images of the MnO_2 nanotubes. (D) Electron diffraction pattern recorded from the end of the nanotube shown in image C.

lower than the stoichiometric ratio (*i.e.*, 3) in eq 1, only nanosheet-based δ-MnO_2 microflowers can be formed, for example, at [HCl]/[MnO_4^-] = 0.05/0.05 = 1 (Figure S5A and the green curve in Figure S5E, Supporting Information). When [HCl]/[MnO_4^-] increases to 2 (that is still lower than 3), the product is dominated by α-MnO_2 nanowires (Figure S5B and the blue curve in Figure S5E, Supporting Information). The difference between these two samples indicates that the redox reaction between MnO_4^- and HCl can occur to form solid MnO_2 regardless of the acidity and that the δ- to α-MnO_2 phase transition requires a high enough acidity of the reaction solutions. When [HCl]/[MnO_4^-] reaches 4, the resulting product is composed of pure α-MnO_2 nanotubes (Figure 1F), indicating the high acidity is beneficial for the ripening process to convert the core/shell nanowires to single-crystalline nanotubes. As shown in Figures S5C and S5D (Supporting Information), further increase of the acidity (*e.g.*, [HCl]/[MnO_4^-] = 8) leads to the formation of single-crystalline α-MnO_2 nanowires with diameters much less than the nanotubes shown in Figure 1F.

Proposed Mechanism for the Nanophase Transition. The characterization results of the products formed at different times and reaction conditions confirm that microflowers made of δ-MnO_2 nanosheets can be formed once the reaction is initiated regardless of the reaction conditions. The nanosheets exhibit typical thicknesses of 3−4 nm and consist of tiny crystalline domains with sizes of several nanometers (Figures 6A and 3C). Owing to the small size of the crystalline domains, the δ-MnO_2 nanosheets are not stable under high temperature and high acidity and they tend to transform into α-MnO_2 domains with large sizes. As a result, such a phase transition initiates the formation of α-MnO_2 nuclei in the nanosheets when the temperature and acidity of the reaction solution are high enough. Because α-MnO_2 is more thermodynamically stable than δ-MnO_2 in the hot and acidic environment, the δ-MnO_2 nanodomains in the nanosheets diffuse to the stable α-MnO_2 nuclei followed by a phase transition and anisotropic growth of the α-MnO_2 nuclei into one-dimensional nanowires (Figure 6B). This diffusion and phase transition process continues until all the nanosheets are consumed. During this process, the α-MnO_2 nanodomains on the surfaces of the resulting nanowires undergo an Ostwald ripening process to fuse them into highly crystalline (even single crystalline) sheaths due to their direct contact with the reaction solution that can promote the movement and recrystallization of the surface α-MnO_2 nanodomains. In contrast, the nanodomains in the interior of the nanowires are relatively unlikely to follow a ripening process. The different activity of nanodomains on

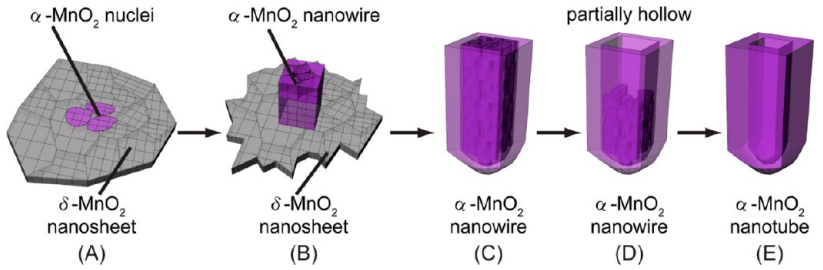

Figure 6. Proposed mechanism responsible for the nanophase transition from δ-MnO_2 nanosheets to α-MnO_2 nanowires and single-crystalline nanotubes.

the surfaces and in the centers of the nanowires toward the Ostwald ripening process leads to the formation of core/shell nanowires made of single-crystalline sheaths and polycrystalline cores (Figure 6C). When the nanowires are continuously heated in the acidic environment, the small crystalline nanodomains can also undergo a slow ripening process due to the contact between the ends of the nanowires with the reaction solution (Figure 6D). This ripening leads the nanodomains to recrystallize and grow into the single crystalline sheaths, resulting in the formation of single crystalline nanotubes (Figure 6E). Because the reaction solution can only contact the core nanodomains from the ends of the nanowires to promote the Ostwald ripening process, the transformation of nanowires to nanotubes takes much longer time than the formation of nanowires.

Lithium–Air Batteries with the Use the Synthesized MnO_2 Nanostructures. Because of the unique crystalline structures, MnO_2 has been widely studied as active components in electrochemical energy storage devices.[1,5,8] We have synthesized high-quality nanosheet-based δ-MnO_2 microflowers (Figure 1A), α-MnO_2 core/shell nanowires with highly crystalline shells, and cores composed of small crystalline domains (Figure 1D), and single-crystalline α-MnO_2 nanotubes (Figure 1F) by using the microwave-assisted hydrothermal approach. The purity of the crystalline phase and morphology of these samples lends them as ideal materials for studying the relationship between device performance and parameters of the MnO_2 particles. For example, the synthesized MnO_2 powders are mixed with carbon black and polyvinylidene fluoride (PVDF) in a solvent (*e.g.*, propylene carbonate + acetone) and cast to form air cathodes for lithium–air batteries. In a typical battery cell, the cathode (in a circular shape with a diameter of 12.7 mm and a thickness of ~25 μm) is separated from the lithium–metal anode by a glass fiber separator soaked with 1.0 M solution of $LiPF_6$ in propylene carbonate (PC). The whole system is sealed in a glass cell filled with pure oxygen for performance evaluation. Despite reported complications of carbonate electrolytes,[35,36] MnO_2 appears uniquely effective for the oxygen reduction and evolution reactions in Li–O_2 cells.[5,37] Figure 7A represents the dependence of voltage on time for the typical lithium–air batteries

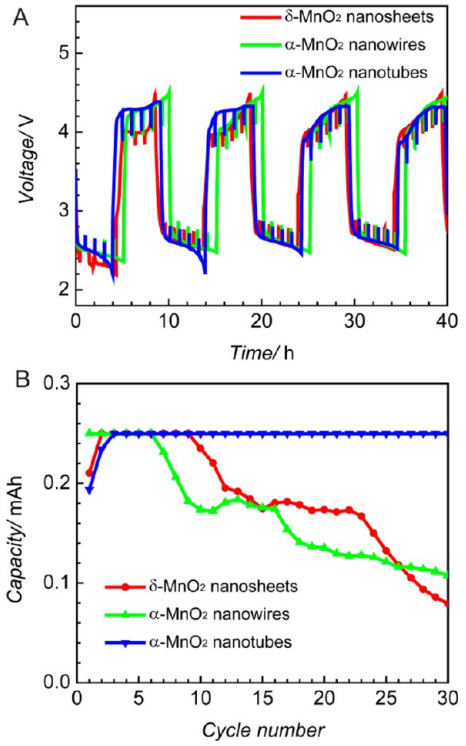

Figure 7. Electrochemical characterization of the lithium–air battery cells with the incorporation of MnO_2 nanostructures shown in Figures 1A (δ-MnO_2 nanosheets), 1D (α-MnO_2 nanowires), and 1F (α-MnO_2 nanotubes) into the air cathodes. (A) Recorded voltage as a function of time during the initial discharge/charge cycles. (B) Variation of the discharge capacity against the cycle number.

during the first four discharge/charge cycles. The cutoff voltages for discharge and charge are set at 2.2 and 4.5 V, respectively. The maximum time for each discharging and charging is 5 h. The current remains constant at 0.05 mA that translates to a current density of 0.04 mA·cm^{-2}. The vertical spikes presented at the discharge and charge plateaus correspond to the voltage changes when the area specific impedance (ASI) of the system is measured periodically during the discharge/charging cycles. The larger amplitude of the spike indicates the system has a higher resistance. The resistances of the cells containing α-MnO_2 nanotubes (blue curve), α-MnO_2 nanowires (green curve), and δ-MnO_2 nanosheets (red curve) are comparable. In contrast to the control cell without MnO_2 (Figure S6,

Supporting Information) that survives only one or two discharge/charge cycles, all the battery cells containing the synthesized MnO_2 nanostructures exhibit significantly improved stability for many operation cycles. The discharge capacities of battery cells made of different MnO_2 particles are plotted in Figure 7B as a function of cycle number. Their capacities increase and reach the highest value of 0.25 mAh after the first 2−3 cycles. The capacities of the batteries with the δ-MnO_2 nanosheets and α-MnO_2 core/shell nanowires start to decrease at cycle number of 10 and 7, respectively. In contrast, the battery made of single-crystalline α-MnO_2 nanotubes remains the highest capacity for at least 30 cycles (*i.e.*, the maximum number evaluated in our experiments). The charge capacity of this battery also shows much better stability than the other two batteries (Figure S7, Supporting Information). Regardless of the crystallinity and morphology of the MnO_2 particles, the lithium−air batteries with the MnO_2 particles exhibit much higher performance in terms of both discharge and charge capacities in comparison with the battery cell without MnO_2, indicating the MnO_2 particles indeed play an important role in catalyzing the electrochemical reactions on the oxygen cathodes. Previous studies have shown that MnO_2 nanostructures can be used as low-cost catalysts for oxygen reduction reaction in alkaline media and their catalytic activities depend on their crystallographic structures following an order of α- > β- > γ-MnO_2.[38] This order is consistent with our observation, that is, the electrodes incorporated with α-MnO_2 nanotubes exhibit much better performance than the electrodes without MnO_2 and the electrodes made of δ-MnO_2 nanosheets. The lower catalytic activity of the δ-MnO_2 nanosheets than the α-MnO_2 nanotubes might be ascribed to the low crystallinity and small size domains in the δ-MnO_2 nanosheets. In addition, the morphological dependence reveals that MnO_2 nanostructures with high surface areas outperform the counterpart particles with lower surface areas.[38] Therefore, it is reasonable to observe that the electrodes with the polycrystalline α-MnO_2 nanowires performed worse than the single crystalline α-MnO_2 nanotubes because the α-MnO_2 nanotubes can expose higher surface areas to the surrounding electrolyte. Moreover, the conductivity of Li^+ ions and electrons in the single crystalline nanotubes is higher than that in the polycrystalline nanowires, benefitting the charge-transfer reactions to enhance catalytic performance. Figure S8 (Supporting Information) presents the SEM images of different electrodes after the batteries have been measured for 30 cycles and completely discharged. Although the electrode without MnO_2 and those with δ-MnO_2 nanosheets and α-MnO_2 nanowires exhibit similar morphology, there are individual microparticles formed on the α-MnO_2 nanotubes-based electrode. Even though the exact composition of the microparticles cannot be precisely characterized, they are most likely the discharge products. Because of the high catalytic activity of the α-MnO_2 nanotubes, the discharge products tend to form only at the active sites of the α-MnO_2 nanotubes. In contrast, the discharge products are formed on all the electrically conductive surfaces including the porous carbon matrix because the low catalytic activity of the δ-MnO_2 nanosheets and the α-MnO_2 nanowires cannot provide selective deposition of the discharge products. Such nonselective deposition of the discharge products can clog the pores in the oxygen cathodes of the lithium−air batteries, leading them to quickly die until the pores are completely clogged. As a result, the selective deposition of discharge products prompted by the high catalytic activity is responsible for the enhanced stability of the batteries with the α-MnO_2 nanotubes-based electrodes.

CONCLUSION

Although MnO_2 nanoparticles can exhibit a large variety of crystallographic structures (*e.g.*, α, β, δ, γ, and λ forms) and morphologies, controlled synthesis of nanostructured MnO_2 with high crystalline purity and uniform morphology is possible. For example, high-quality nanosheet-based δ-MnO_2 microflowers, α-MnO_2 nanowires, and α-MnO_2 nanotubes have been synthesized in large quantity through a microwave-assisted hydrothermal reduction of potassium permanganate in the presence of hydrochloric acid. Time-dependent studies reveal that the chemical reaction determines the formation of δ-MnO_2 microflowers, and the two-step Ostwald ripening process dominates the crystalline and morphological transition from the δ-MnO_2 nanosheets to α-MnO_2 nanowires and nanotubes. This understanding can help us better control reaction conditions to synthesize MnO_2 nanoparticles with more precisely tailored properties and achieve better performance in their applications. For instance, the single crystalline α-MnO_2 nanotubes exhibit much better performance to catalyze the electrochemical processes involved in lithium−air batteries, leading to a significant improvement in energy capacity and stability.

METHODS

Synthesis of MnO_2 Nanostructures. The nanostructured MnO_2 were synthesized in aqueous solutions using a CEM Discover microwave reactor system. $KMnO_4$ and concentrated HCl (37% in v/v) were purchased from Sigma-Aldrich and used without further purification. In a typical procedure, $KMnO_4$

(52.6 mg, 0.33 mmol) and 1.2 M HCl solution (1 mL) were sequentially added to deionized water (5 mL) in a 10-mL microwave reaction tube. The solution was then heated to 150 °C for 6 h under the sealed vessel mode with microwave irradiation. The resulting brownish-black solid product was centrifuged, washed with deionized water, and dried at 60 °C in an oven. For the time-dependence study, the reaction was stopped at different times and the corresponding brownish-black precipitates were obtained accordingly.

Characterization of the Synthesized MnO_2 Nanostructures. X-ray diffraction patterns were collected with a high-energy (115 keV, λ = 0.10798 Å) synchrotron X-ray beam at 11-ID-C of Advanced Photon Source (APS). Scanning electron microscopy (SEM) images were recorded on a JEOL JSM-7500F field emission scanning electron microscope. Transmission electron microscopy (TEM) images and electron diffraction patterns were taken on a JEOL JEM-2100F microscope operating at a voltage of 200 kV.

Assembly of Lithium–Air (Oxygen) Battery Cells and Performance Evaluation. Oxygen cathodes incorporating the as-synthesized MnO_2 nanostructures were first prepared. In a typical process, the as-prepared MnO_2 powders (20 mg), carbon black (Super P Li, 55 mg), polyvinylidene fluoride (PVDF, Kynar, 75 mg), and propylene carbonate (PC, 275 mg) were mixed in acetone (3 g), and the mixture was continuously stirred overnight. Casting the well-mixed paste resulted in the formation of a film with a thickness of ~25 μm, and the film was then dried in a desiccator. The dry film was punched into circular pieces with a diameter of 12.7 mm to serve as the air cathodes in lithium–air battery cells. The complete assembly of a lithium–air battery cell consisted of a lithium metal anode, a glass-fiber separator wetted with electrolyte (1 M $LiPF_6$ in PC), and a circular air electrode supported with an aluminum grid. The cell layout and more information about cell assembly was reported previously.[39] All the processes of assembling the battery cell and sealing it in a glass tube was carried out in a glovebox filled with argon. The enclosed glass cell was then filled with pure oxygen for 30 min before electrochemical evaluation. The electrochemical evaluation was carried out with a Maccor tester system. A current of 0.05 mA was kept constant during the measurement, while the cut off voltages for discharge and charge cycles were 2.2 and 4.5 V, respectively. The maximum duration for each discharge and charge was limited by 5 h. Area specific impedance (ASI) of the system was periodically measured during the discharge and charge cycles.

Conflict of Interest: The authors declare no competing financial interest.

Acknowledgment. Use of the Center for Nanoscale Materials and Advanced Photon Source (Beamline 11-ID-C) at Argonne National Laboratory was supported by the U.S. Department of Energy, Office of Science of Basic Energy Sciences, under Contract DE-AC02-06CH11357.

Supporting Information Available: Absorption spectra of reaction solutions obtained at different reaction times; details on the influence of reaction temperature, pressure, and concentration of HCl on the MnO_2 nanostructures by SEM, XRD, and TEM; electrochemical characterization of a lithium–air battery cell using an air cathode without MnO_2 nanostructures; details on the variation of charge capacity against the cycle number; SEM images of the cathode electrodes after measurements. This material is available free of charge *via* the Internet at http://pubs.acs.org.

REFERENCES AND NOTES

1. Thackeray, M. M. Manganese Oxides for Lithium Batteries. *Prog. Solid State Chem.* **1997**, *25*, 1–71.
2. Thackeray, M. M.; David, W. I. F.; Bruce, P. G.; Goodenough, J. B. Lithium Insertion into Manganese Spinels. *Mater. Res. Bull.* **1983**, *18*, 461–472.
3. Li, B. X.; Rong, G. X.; Xie, Y.; Huang, L. F.; Feng, C. Q. Low-Temperature Synthesis of α-MnO_2 Hollow Urchins and Their Application in Rechargeable Li^+ Batteries. *Inorg. Chem.* **2006**, *45*, 6404–6410.
4. Thapa, A. K.; Ishihara, T. Mesoporous α-MnO_2/Pd Catalyst Air Electrode for Rechargeable Lithium–Air Battery. *J. Power Sources* **2011**, *196*, 7016–7020.
5. Débart, A.; Paterson, A. J.; Bao, J.; Bruce, P. G. α-MnO_2 Nanowires: A Catalyst for the O_2 Electrode in Rechargeable Lithium Batteries. *Angew. Chem., Int. Ed.* **2008**, *47*, 4521–4524.
6. Cheng, H.; Scott, K. Carbon-Supported Manganese Oxide Nanocatalysts for Rechargeable Lithium–Air Batteries. *J. Power Sources* **2010**, *195*, 1370–1374.
7. Li, J.; Wang, N.; Zhao, Y.; Ding, Y.; Guan, L. MnO_2 Nanoflakes Coated on Multi-walled Carbon Nanotubes for Rechargeable Lithium–Air Batteries. *Electrochem. Commun.* **2011**, *13*, 698–700.
8. Wei, W.; Cui, X.; Chen, W.; Ivey, D. G. Manganese Oxide-Based Materials as Electrochemical Supercapacitor Electrodes. *Chem. Soc. Rev.* **2011**, *40*, 1697–1721.
9. Lang, X. Y.; Hirata, A.; Fujita, T.; Chen, M. W. Nanoporous Metal/Oxide Hybrid Electrodes for Electrochemical Supercapacitors. *Nat. Nanotechnol.* **2011**, *6*, 232–236.
10. Girishkumar, G.; McCloskey, B.; Luntz, A. C.; Swanson, S.; Wilcke, W. Lithium-Air Battery: Promise and Challenges. *J. Phys. Chem. Lett.* **2010**, *1*, 2193–2203.
11. Goodenough, J. B.; Kim, Y. Challenges for Rechargeable Li Batteries. *Chem. Mater.* **2010**, *22*, 587–603.
12. Wagner, F. T.; Lakshmanan, B.; Mathias, M. F. Electrochemistry and the Future of the Automobile. *J. Phys. Chem. Lett.* **2010**, *1*, 2204–2219.
13. Devaraj, S.; Munichandraiah, N. Effect of Crystallographic Structure of MnO_2 on Its Electrochemical Capacitance Properties. *J. Phys. Chem. C* **2008**, *112*, 4406–4417.
14. Jintao, Z.; Wei, C.; Jianwen, J.; Zhao, X. S. Synthesis, Characterization and Capacitive Performance of Hydrous Manganese Dioxide Nanostructures. *Nanotechnology* **2011**, *22*, 125703.
15. Brousse, T.; Toupin, M.; Dugas, R.; Athouel, L.; Crosnier, O.; Belanger, D. Crystalline MnO_2 as Possible Alternatives to Amorphous Compounds in Electrochemical Supercapacitors. *J. Electrochem. Soc.* **2006**, *153*, A2171–A2180.
16. Wang, X.; Yuan, A.; Wang, Y. Supercapacitive Behaviors and Their Temperature Dependence of Sol-Gel Synthesized Nanostructured Manganese Dioxide in Lithium Hydroxide Electrolyte. *J. Power Sources* **2007**, *172*, 1007–1011.
17. Li, W. N.; Yuan, J. K.; Shen, X. F.; Gomez-Mower, S.; Xu, L. P.; Sithambaram, S.; Aindow, M.; Suib, S. L. Hydrothermal Synthesis of Structure- and Shape-Controlled Manganese Oxide Octahedral Molecular Sieve Nanomaterials. *Adv. Funct. Mater.* **2006**, *16*, 1247–1253.
18. Qiu, G.; Huang, H.; Dharmarathna, S.; Benbow, E.; Stafford, L.; Suib, S. L. Hydrothermal Synthesis of Manganese Oxide Nanomaterials and Their Catalytic and Electrochemical Properties. *Chem. Mater.* **2011**, *23*, 3892–3901.
19. Ai, Z.; Zhang, L.; Kong, F.; Liu, H.; Xing, W.; Qiu, J. Microwave-Assisted Green Synthesis of MnO_2 Nanoplates with Environmental Catalytic Activity. *Mater. Chem. Phys.* **2008**, *111*, 162–167.
20. Zhou, M.; Zhang, X.; Wei, J. M.; Zhao, S. L.; Wang, L.; Feng, B. X. Morphology-Controlled Synthesis and Novel Microwave Absorption Properties of Hollow Urchinlike α-MnO_2 Nanostructures. *J. Phys. Chem. C* **2011**, *115*, 1398–1402.
21. Ju, S. H.; Kang, Y. C. Nano-sized Manganese Oxide Particles Prepared by Low-Pressure Spray Pyrolysis Using FEAG Process. *Mater. Res. Bull.* **2008**, *43*, 590–600.
22. Cheng, J. H.; Shao, G. A.; Yu, H. J.; Xu, J. J. Excellent Catalytic and Electrochemical Properties of the Mesoporous MnO_2 Nanospheres/Nanosheets. *J. Alloys Compd.* **2010**, *505*, 163–167.
23. Nam, H.-S.; Yoon, J.-K.; Ko, J. M.; Kim, J.-D. Electrochemical Capacitors of Flower-like and Nanowire Structured MnO_2 by a Sonochemical Method. *Mater. Chem. Phys.* **2010**, *123*, 331–336.
24. Zhao, J.; Tao, Z.; Liang, J.; Chen, J. Facile Synthesis of Nanoporous γ-MnO_2 Structures and Their Application in Rechargeable Li-Ion Batteries. *Cryst. Growth Des.* **2008**, *8*, 2799–2805.

25. Li, Q.; Olson, J. B.; Penner, R. M. Nanocrystalline α-MnO_2 Nanowires by Electrochemical Step-Edge Decoration. *Chem. Mater.* **2004**, *16*, 3402–3405.
26. Xia, H.; Feng, J.; Wang, H.; Lai, M. O.; Lu, L. MnO_2 Nanotube and Nanowire Arrays by Electrochemical Deposition for Supercapacitors. *J. Power Sources* **2010**, *195*, 4410–4413.
27. Wang, X.; Li, Y. Synthesis and Formation Mechanism of Manganese Dioxide Nanowires/Nanorods. *Chem.—Eur. J.* **2003**, *9*, 300–306.
28. Ma, R.; Bando, Y.; Zhang, L.; Sasaki, T. Layered MnO_2 Nanobelts: Hydrothermal Synthesis and Electrochemical Measurements. *Adv. Mater.* **2004**, *16*, 918–922.
29. Feng, Q. Synthesis and Applications of Manganese Oxide Nanotubes. In *Inorganic and Metallic Nanotubular Materials*; Kijima, T., Ed.; Springer: Berlin/Heidelberg:, 2010; Vol. 117, pp 73−82.
30. Li, H.; Wang, W.-l.; Pan, F.; Xin, X.; Chang, Q.; Liu, X. Synthesis of Single-Crystalline α-MnO_2 Nanotubes and Structural Characterization by HRTEM. *Mater. Sci. Eng., B* **2011**, *176*, 1054–1057.
31. Luo, J.; Zhu, H. T.; Fan, H. M.; Liang, J. K.; Shi, H. L.; Rao, G. H.; Li, J. B.; Du, Z. M.; Shen, Z. X. Synthesis of Single-Crystal Tetragonal α-MnO_2 Nanotubes. *J. Phys. Chem. C* **2008**, *112*, 12594–12598.
32. Opembe, N. N.; King'ondu, C. K.; Espinal, A. E.; Chen, C.-H.; Nyutu, E. K.; Crisostomo, V. M.; Suib, S. L. Microwave-Assisted Synthesis of Manganese Oxide Octahedral Molecular Sieve (OMS-2) Nanomaterials under Continuous Flow Conditions. *J. Phys. Chem. C* **2010**, *114*, 14417–14426.
33. Polshettiwar, V.; Nadagouda, M. N.; Varma, R. S. Microwave-Assisted Chemistry: A Rapid and Sustainable Route to Synthesis of Organics and Nanomaterials. *Aust. J. Chem.* **2009**, *62*, 16–26.
34. Dallinger, D.; Kappe, C. O. Microwave-Assisted Synthesis in Water as Solvent. *Chem. Rev.* **2007**, *107*, 2563–2591.
35. Freunberger, S. A.; Chen, Y.; Peng, Z.; Griffin, J. M.; Hardwick, L. J.; Barde, F.; Novak, P.; Bruce, P. G. Reactions in the Rechargeable Lithium-O_2 Battery with Alkyl Carbonate Electrolytes. *J. Am. Chem. Soc.* **2011**, *133*, 8040–8047.
36. McCloskey, B. D.; Bethune, D. S.; Shelby, R. M.; Girishkumar, G.; Luntz, A. C. Solvents' Critical Role in Nonaqueous Lithium-Oxygen Battery Electrochemistry. *J. Phys. Chem. Lett.* **2011**, *2*, 1161–1166.
37. Giordani, V.; Freunberger, S. A.; Bruce, P. G.; Tarascon, J. M.; Larcher, D. H_2O_2 Decomposition Reaction as Selecting Tool for Catalysts in Li-O_2 Cells. *Electrochem. Solid State Lett.* **2010**, *13*, A180–A183.
38. Cheng, F.; Su, Y.; Liang, J.; Tao, Z.; Chen, J. MnO_2-Based Nanostructures as Catalysts for Electrochemical Oxygen Reduction in Alkaline Media. *Chem. Mater.* **2009**, *22*, 898–905.
39. Truong, T. T.; Qin, Y.; Ren, Y.; Chen, Z.; Chan, M. K.; Greeley, J. P.; Amine, K.; Sun, Y. Single-Crystal Silicon Membranes with High Lithium Conductivity and Application in Lithium-Air Batteries. *Adv. Mater.* **2011**, *23*, 4947–4952.